processes

MDPI

Article

Global Modeling of Heat-Integrated Distillation Column Based on Limited Local Measurements

Lin Cong [1,*], Dengpan Liu [1] and Huaizhi Ling [2]

[1] College of Control Science and Engineering, China University of Petroleum (East China), Qingdao 266580, China
[2] School of Geosciences, China University of Petroleum (East China), Qingdao 266580, China
* Correspondence: conglin@upc.edu.cn

Abstract: The heat-integrated distillation column (HIDiC) has more energy-saving potential than conventional distillation columns. However, its nonlinearity and coupling effects pose significant challenges for the online operation of the HIDiC. To overcome these challenges, it becomes necessary to utilize accurate nonlinear models for design optimization or control schemes. Traditional modeling methods require extensive tray information, implying the impractical use of numerous sensors in real-world applications. This paper proposes a modeling approach for the HIDiC based on a limited number of measurements. It only requires the measurement of a finite amount of tray information to construct a global model of the HIDiC. This method serves as an online observer, providing real-time information about the entire column, and also enables the prediction of tray concentration changes. The proposed model forms the basis for developing model-based online monitoring and control schemes. Experimental simulation results demonstrate that the proposed method achieves high accuracy in global observation and prediction for the HIDiC.

Keywords: heat-integrated distillation column; nonlinear modeling; online observer; nonlinear wave model; mass transfer mechanisms

Citation: Cong, L.; Liu, D.; Ling, H. Global Modeling of Heat-Integrated Distillation Column Based on Limited Local Measurements. *Processes* **2024**, *12*, 484. https://doi.org/10.3390/pr12030484

Academic Editor: Iqbal M. Mujtaba

Received: 6 February 2024
Revised: 23 February 2024
Accepted: 25 February 2024
Published: 27 February 2024

1. Introduction

Distillation is the most widely used mass transfer unit operation in petroleum refining, petrochemical, and other industrial processes. It is also one of the most energy-consuming unit operations in the petrochemical industry [1]. Statistical data indicate that approximately 40% to 50% of the total energy consumption in the petroleum and chemical industries is attributed to distillation processes [2–4]. This process wastes significant resources such as water, coal, and gas every year. The accumulated energy losses become immeasurable. In response to this challenge, heat-integrated distillation technology has been introduced as an innovative and energy-efficient technique. It can achieve energy savings of at least 30% compared to traditional distillation columns with proper process and control design in numerous applications [1]. Therefore, studying the modeling and control design of heat-integrated distillation processes is significant for reducing carbon emissions in human activities [5].

As shown in Figure 1, the heat-integrated distillation column (HIDiC) is divided into rectifying and stripping sections. The heat-integrated distillation column separates the conventional distillation column into these two parts. Between these two sections, a compressor and a throttle valve are introduced, allowing for the temperature in the rectifying section to be higher than that in the stripping section and facilitating heat transfer from the rectifying column to the stripping column. With a well-thought-out design, it is possible to reduce the burden on the condenser and reboiler significantly. Therefore, the internal heat transfer dramatically enhances energy efficiency despite the increased energy consumption of the compressor.

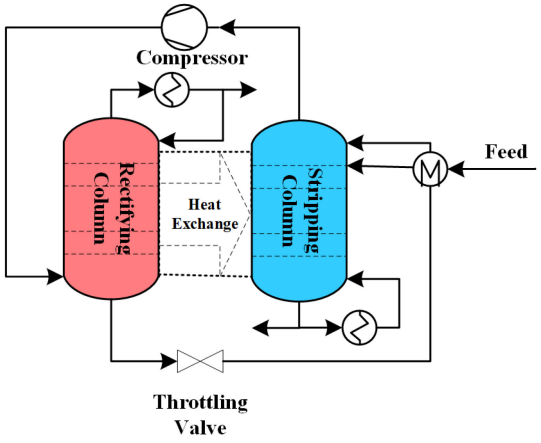

Figure 1. Schematic diagram of the HIDiC.

Numerous scholars have conducted extensive research to explore the feasibility of heat-integrated distillation energy-saving technology. Much of this research focuses on the conceptual design of heat-integrated distillation columns in different scenarios, such as standard forms of heat-integrated distillation columns [6–9], heat-integrated pressure-swing columns [10–12], heat-integrated extractive distillation columns [13–16], heat-integrated air-separation columns [17–20], and heat-integrated reactive distillation columns [21–24]. Most of the works are primarily implemented through specific process simulation software. This research demonstrates the promising energy-saving prospects of heat-integrated distillation technology in various scenarios.

However, due to the thermal coupling between the rectifying and stripping sections, the HIDiC exhibits complex dynamic characteristics and strong nonlinearity, posing significant challenges for online control [25,26]. Conventional PID control or control schemes based on linear approximation models often require extensive fine-tuning of control loops and have strict limitations on operating ranges. Therefore, there is a significant need for control design based on nonlinear models [13,27,28].

Hence, some scholars have focused on the nonlinear modeling research of the HIDiCs. The primary modeling approach involves mechanistic modeling based on MESH equations (mass balance equation, phase-equilibrium equation, molar fraction summation equation, and heat-balance equation). The mechanistic modeling research encompasses various scenarios, including standard HIDiCs [6,29], heat-integrated reactive columns [23,30,31], heat-integrated pressure-swing columns [32–34], heat-integrated air-separation columns [19,35–37], and more. The core of mechanistic modeling lies in describing the conditions for each tray, involving many differential and algebraic equations. However, obtaining process variable information for each tray is impractical, as installing measurement sensors on every tray in the actual process is not feasible.

Therefore, from a practical perspective, a relatively accurate nonlinear model for the HIDiC is needed. Additionally, this model should not impose excessively stringent requirements on the global nature of process variables to avoid the dilemma of needing to install a large number of sensors. Our previous work proposed a nonlinear wave model to describe the concentration distribution curve for the entire column in an HIDiC [20,38]. This approach considers the concentration distribution curve as a whole. While ensuring a certain level of accuracy, this model is more simplified than the mechanistic model. However, this modeling method is based on a data regression approach to establish descriptive functions, which has limitations and lacks a mechanistic basis, potentially leading to significant model errors in certain situations. Furthermore, although this model significantly reduces the number of differential equations, it still requires a substantial amount of process variable information.

To address the issues above, this paper first explores the distribution patterns of concentrations on each tray of an HIDiC based on mass transfer mechanisms. Consequently, a

novel functional form for describing the concentration distribution curves is established. The proposed function indicates the mechanistic interconnections among the concentrations on different trays, and these connections can be quantitatively described using certain function expressions. Simultaneously, a formula for the moving velocity of the concentration distribution curves is derived, allowing our proposed method to describe both static and dynamic behaviors. The curve description function and its velocity expression form the basis for establishing a nonlinear model based on mass transfer mechanisms. Furthermore, based on this fixed form of concentration distribution curve function, a global observation method is introduced using a limited number of tray temperature measurements. By utilizing temperature information from a few specific trays, critical parameters from the concentration distribution curve function can be extracted. Subsequently, global information on all trays can be obtained based on the established model. In simulation experiments, experimental comparisons are conducted between the proposed, mechanistic, and previous wave models. The results indicate that the proposed modeling method achieves high accuracy, validating its effectiveness.

2. Nonlinear Modeling Based on Mass Transfer Mechanisms

2.1. Mechanistic Model of an HIDiC

This paper takes the benzene–toluene system as an example. It begins by briefly introducing the mechanistic model of an HIDiC [6], which will serve as the baseline for subsequent simulation comparisons.

The heat-coupling equations encompass the thermal-coupling relationship between the rectifying column and the stripping column and the relationships between the tray temperature, the concentration, and the pressure. The equation is formulated as follows:

$$Q_j = UA(T_j - T_{j+f-1})\ j = 1, \cdots, f-1 \tag{1}$$

$$T_j = b/(a - Lnp_{vp,j}) - c \tag{2}$$

$$p_{vp,j} = p/[X_j + (1 - X_j)/\alpha] \tag{3}$$

where Q represents the heat transfer between coupled trays, j denotes the tray number and the numbering of the trays starts from the top of the column, UA is the heat transfer rate, T is the tray temperature, f represents the feed tray, and a, b, and c are material-related characteristic constants in the Antoine equation. Additionally, $p_{vp,j}$ is the saturation vapor pressure, p is the internal pressure of the column, X is the liquid-phase molar fraction, and α is the relative volatility. Note that p refers to the pressure of the rectifying section or the stripping section. We assume that the pressure inside each column is uniform and do not consider pressure differentials between individual trays.

The liquid-phase molar flow rate for each tray in the rectifying section can be expressed as:

$$L_j = \sum_{k=1}^{j} Q_k/\lambda, \qquad (j = 1, \ldots, f-1) \tag{4}$$

where λ represents the latent heat of vaporization.

The vapor-phase molar flow rate for each tray in the rectifying section can be expressed as:

$$V_{j+1} = V_1 + L_j, \qquad (j = 1, \ldots, f-1) \tag{5}$$

The vapor-phase molar flow rate for the first tray in the rectifying section is given by:

$$V_1 = F(1 - q) \tag{6}$$

where F is the feed rate, and q is the feed thermal condition.

The liquid-phase flow rate for each tray in the stripping section is:

$$L_{f+j-1} = L_{f-1} + Fq - \sum_{k=1}^{j} Q_k/\lambda, \qquad (j = 1, \ldots, f-2) \tag{7}$$

$$L_n = F - V_1 \tag{8}$$

The expression for the vapor-phase flow rate for each tray in the stripping section is:

$$V_{f+j} = V_f - F(1-q) - \sum_{k=1}^{j} Q_k/\lambda\ . \qquad (j = 1, \ldots, f-2) \tag{9}$$

The vapor–liquid equilibrium equation describes the relationship between the vapor and liquid molar fractions of the components at each tray. The equation is formulated as follows:

$$Y_j = \alpha X_j/[(\alpha-1)X_j + 1]\ j = 1, 2, \cdots, n \tag{10}$$

where Y is the vapor-phase molar fraction.

The component balance equation describes the material conservation relationship at each tray in the HIDiC. The specific equation forms are as follows:

$$H\frac{dX_1}{dt} = V_2Y_2 - V_1Y_1 - L_1X \tag{11}$$

$$H\frac{dX_j}{dt} = V_{j+1}Y_{j+1} - V_jY_j - L_jX_j + L_{j-1}X_{j-1}\ j = 2, \cdots, n-1\ and\ j \neq f \tag{12}$$

$$H\frac{dX_f}{dt} = V_{f+1}Y_{f+1} - V_fY_f - L_fX_f + L_{f-1}X_{f-1} + FZ_f \tag{13}$$

$$H\frac{dX_n}{dt} = -V_nY_n - L_nX_n + L_{n-1}X_{n-1} \tag{14}$$

where H is the liquid holdup on the tray, and Z_f represents the feed composition.

2.2. The Nonlinear Wave Model of the HIDiC

In our previous work, we established a nonlinear reduced-order wave model, treating the concentration distribution curve as a whole to study the static and dynamic characteristics of the HIDiC [20,38]. As shown in Figure 2, the concentration distribution curve moves within the column when operating conditions change. Profile 1 represents the system's initial equilibrium state. After changes in the operating conditions, the concentration distribution curve gradually moves to the position of Profile 2, indicating that the system has reached a new equilibrium state.

Although the shape of the concentration distribution curve changes during dynamic processes, it consistently maintains the configuration of an S-shaped hyperbolic curve. Therefore, we can use the following descriptive function to represent the concentration distribution curve:

$$\hat{X}_j = X_{r\_\min} + \frac{X_{r\_\max} - X_{r\_\min}}{1 + e^{-k_r(j-S_1)}}\ j = 1, 2, \cdots, f-1 \tag{15}$$

$$\hat{X}_j = X_{s\_\min} + \frac{X_{s\_\max} - X_{s\_\min}}{1 + e^{-k_s(j-S_2)}}\ j = f, f+1, \cdots, n \tag{16}$$

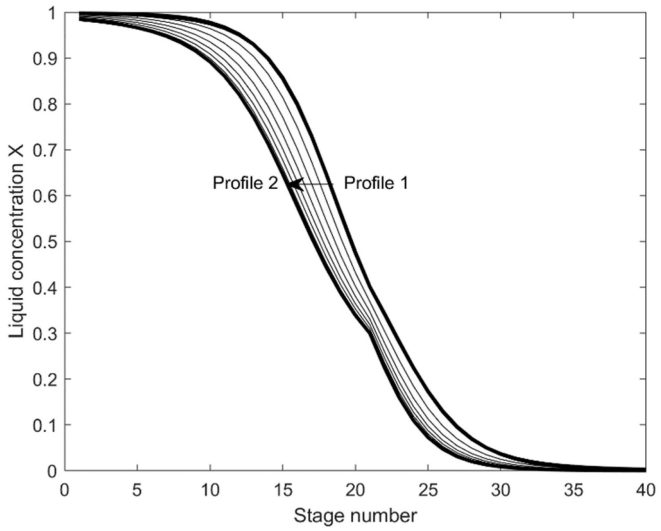

Figure 2. The movement of the concentration distribution curve.

Here, $\hat{X}_j$ represents the observed concentration value at the j-th tray, and $X_{r\_\max}$, $X_{r\_\min}$, k_r, $X_{s\_\max}$, $X_{s\_\min}$, k_s are the curve parameters. $X_{r\_\max}$ and $X_{s\_\max}$ are the maximum approximating concentrations in the rectifying and stripping sections, respectively, while $X_{r\_\min}$ and $X_{s\_\min}$ are the maximum approximating concentrations in the rectification and stripping sections, respectively. k_r and k_s represent the slope characterization at the inflection point positions. S_1 and S_2 denote the inflection point positions of the concentration distribution curves in the rectifying and stripping sections, respectively, corresponding to the locations with the maximum absolute slope. The curve parameters are determined based on the concentration values of each tray using identification methods, essentially relying on a data regression curve fitting approach and lacking specific theoretical support.

Furthermore, we typically use the inflection points to represent the position of the concentration distribution curves. By deriving the equation for the movement speed of these inflection points, the dynamic behavior of the HIDiC can be characterized. The specific equation form is as follows:

$$\frac{dS_1}{dt} = \frac{\frac{1}{H}(-V_1Y_1 + V_fY_f - L_{f-1}X_{f-1})}{-\sum_{j=1}^{f-1} \frac{k_r(X_{r\_\max} - X_j)(X_j - X_{r\_\min})}{X_{r\_\max} - X_{r\_\min}}} \tag{17}$$

$$\frac{dS_2}{dt} = \frac{\frac{1}{H}(-L_nX_n - V_fY_f + L_{f-1}X_{f-1} + FZ_f)}{-\sum_{j=f}^{n} \frac{k_s(X_{s\_\max} - X_j)(X_j - X_{s\_\min})}{X_{s\_\max} - X_{s\_\min}}} \tag{18}$$

Coupled with certain algebraic equations, a nonlinear reduced-order wave model for the HIDiC can be constructed. While the aforementioned nonlinear model considers some typical features of the HIDiC, it does not explore the mass transfer mechanisms more profoundly. Therefore, to enhance the accuracy of the nonlinear model, further in-depth research into the mass transfer mechanisms of the HIDiC is necessary.

2.3. Nonlinear Modeling Based on Mass Transfer Mechanisms

If there are many trays in a plate tower, and factors, such as vapor holdup and energy loss are neglected, the structure of the plate tower can be approximated as a packed tower [39]. Partial differential equations can represent its mass transfer equations

approximately. First, the simple mass transfer partial differential equation within a small volume unit in the distillation process is expressed as follows:

$$\frac{\partial x}{\partial t} - \frac{\partial x}{\partial s} = -M_{\mathrm{T}}(y^*(x) - y) \tag{19}$$

$$\frac{V}{L}\frac{\partial y}{\partial s} = M_{\mathrm{T}}(y^*(x) - y) \tag{20}$$

where x and y represent the concentrations of the liquid and vapor phases, respectively, M_{T} is the dimensionless mass transfer coefficient, L is the molar flow rate of the liquid phase, V is the molar flow rate of the vapor phase, y^* describes the vapor–liquid equilibrium relationship, and s is the dimensionless spatial coordinate.

Assuming that the process is in a quasi-steady state, i.e., $\partial x/\partial t = 0$, the coordinate system is transformed into a coordinate system $(l - t)$ with a moving speed v. The coordinate transformation is defined as follows:

$$l = s - s' \tag{21}$$

$$s' = \int v dt \tag{22}$$

Substituting Equations (21) and (22) into Equations (19) and (20), we obtain:

$$(1 + v)\frac{\partial x}{\partial l} = M_{\mathrm{T}}(y^*(x) - y) \tag{23}$$

$$\frac{V}{L}(1 + v)\frac{\partial y}{\partial l} = M_{\mathrm{T}}(y^*(x) - y) \tag{24}$$

where $s = s'$ represents the origin of the $l - t$ coordinate system. According to the above equations, we can quickly obtain the following system of equations:

$$l - \int \frac{(1 + v)dx}{M_{\mathrm{T}}(C_1 + y^*(x) - Lx/V)} + C_2 = 0 \tag{25}$$

where C_1 and C_2 are constants resulting from the indefinite integrals. It is challenging to directly solve for the tray concentration from Equation (25). In order to find the concentration expression, this paper adopts a fractional polynomial approximation $y^*(\hat{x}) = \frac{\hat{x}+A}{B\hat{x}+C}$ for the vapor–liquid equilibrium relationship y^*. The integrated function in Equation (25) is handled using a partial fraction decomposition as follows:

$$\frac{(1 + v)}{MT(C_1 + y^*(x) - Lx/V)} = \frac{\hat{x} - m_5}{m_3(\hat{x} - m_1)(\hat{x} - m_2)} \tag{26}$$

where m_1, m_2, m_3, and m_5 represent the parameters in the factorization. Substituting Equation (26) into Equation (25) for integration, the concentration curve description function can be calculated as follows:

$$l - \frac{1}{m_3(m_1 - m_2)}[(m_5 + m_1)\ln(m_1 - \hat{x}) - (m_5 + m_2)\ln(\hat{x} - m_2)] - m_4 = 0 \tag{27}$$

where m_4 represents the constant term generated by the indefinite integral in Equation (25). According to the previously mentioned coordinate transformation relationship, and letting $S = s' + m_4$, $\eta = m_3\ (m_1 - m_2)$, the concentration curve description function can be obtained as follows:

$$l + \frac{1}{\eta}[(m_5 + m_1)\ln(m_1 - \hat{x}) - (m_5 + m_2)\ln(\hat{x} - m_2)] - S = 0 \tag{28}$$

Combining the actual physical meanings of the curve parameters in the HIDiC, the description function of the concentration distribution curve can be expressed in the following form:

$$j + \frac{1}{k_r}[(a_r + X_{r\_\max})\ln(X_{r\_\max} - \hat{X}_j) - (a_r + X_{r\_\min})\ln(\hat{X}_j - X_{r\_\min})] - S_1 = 0 \quad j = 1, 2, \cdots, f-1 \tag{29}$$

$$j + \frac{1}{k_s}[(a_s + X_{s\_\max})\ln(X_{s\_\max} - \hat{X}_j) - (a_s + X_{s\_\min})\ln(\hat{X}_j - X_{s\_\min})] - S_2 = 0 \quad j = f, f+1, \cdots, n \tag{30}$$

where $X_{r\_\max}$, $X_{r\_\min}$, k_r, $X_{s\_\max}$, $X_{s\_\min}$, k_s, S_1, and S_2 have the same physical meanings as the corresponding parameters in the curve description function. The additional parameters a_r and a_s characterize the asymmetrical characteristics of the curve.

In dynamic processes, the fluctuation ranges of parameters $X_{r\_\max}$, $X_{r\_\min}$, k_r, $X_{s\_\max}$, $X_{s\_\min}$, k_s, a_r, and a_s are relatively small. Therefore, in the derivation of the curve movement velocity formula, it can be approximated that the change rate of the above parameters is zero. Based on this assumption, the derivation process can be simplified. The curve parameters are updated online during the dynamic calculation to reduce the errors introduced by this assumption. Following the above assumption, Equations (29) and (30) lead to:

$$\frac{d\hat{X}_j}{dt} = \frac{-k_r}{\frac{a_r + X_{r\_\max}}{X_{r\_\max} - X_j} + \frac{a_r + X_{r\_\min}}{X_j - X_{r\_\min}}} \frac{dS_1}{dt} \quad j = 1, 2, \cdots, f-1 \tag{31}$$

$$\frac{d\hat{X}_j}{dt} = \frac{-k_s}{\frac{a_s + X_{s\_\max}}{X_{s\_\max} - X_j} + \frac{a_s + X_{s\_\min}}{X_j - X_{s\_\min}}} \frac{dS_2}{dt} \quad j = f, f+1, \cdots, n \tag{32}$$

where $\hat{X}_j$ is the observed value of X_j, and it is assumed that $\frac{d\hat{X}_j}{dt} \approx \frac{dX_j}{dt}$. Substituting Equations (31) and (32) into the material conservation equations for both the rectifying and stripping sections of the HIDiC (Equations (11)–(14)), performing summation operations on the trays, and through algebraic transformations, the movement velocity of the concentration distribution curve for the HIDiC can be obtained as follows:

$$\frac{dS_1}{dt} = \frac{-V_1 Y_1 + V_f Y_f - L_{f-1} X_{f-1}}{-H \sum_{j=1}^{f-1} \frac{k_r}{(a_r + X_{r\_\max})/(X_{r\_\max} - X_j) + (a_r + X_{r\_\min})/(X_j - X_{r\_\min})}} \tag{33}$$

$$\frac{dS_2}{dt} = \frac{-V_f Y_f + L_{f-1} X_{f-1} + F Z_f - L_n X_n}{-H \sum_{j=f}^{n} \frac{k_s}{(a_s + X_{s\_\max})/(X_{s\_\max} - X_j) + (a_s + X_{s\_\min})/(X_j - X_{s\_\min})}} \tag{34}$$

Equations (33) and (34), the description functions (Equations (29) and (30)), and the previously mentioned vapor–liquid equilibrium equation, the heat-coupling equation, and the vapor–liquid molar flow rate equation together constitute the nonlinear dynamic model of the HIDiC.

In a simulation example with initial operating conditions, as shown in Table 1, we conducted a simulation comparison of the two nonlinear models (the previous wave model and the new model based on mass transfer mechanisms) for estimating the steady-state tray concentrations.

Figure 3 illustrates the errors between the concentration observations of the two models and the actual concentration (with the mechanistic model as a reference). From the figure, it can be observed that: first, the prediction errors of both models are on the order of 10^{-3} or smaller, indicating high precision in concentration observation for both methods; second, the concentration prediction errors of the new model are significantly

smaller than those of the previous model in the rectifying section, while both methods exhibit similar concentration prediction errors in the stripping section. This situation occurs because the advantage of the non-symmetric characteristics introduced in the new model is more pronounced in the rectifying section, while the significance of the non-symmetry decreases in the stripping section, in this case.

Table 1. Initial operating conditions of the HIDiC.

Stage number (n)	40	Feed thermal condition (q)	0.501
Feed stage (f)	21	Feed flow rate [kmol/h] (F)	100
Feed composition in mole fraction (Z_f)	0.5	Liquid holdup in each stage [kmol] (H)	1.5
Heat transfer rate in each stage [W/K] (UA)	9803	Relative volatility without mismatch (α)	2.317
Antoine equation constants (a)	15.9008	Latent heat of vaporization [J/kmol] (λ)	30001.1
Antoine equation constants (b)	2788.51	Pressure of rectifying section [MPa] (P_r)	0.3387
Antoine equation constants (c)	−52.36	Pressure of stripping section [MPa] (P_s)	0.1013

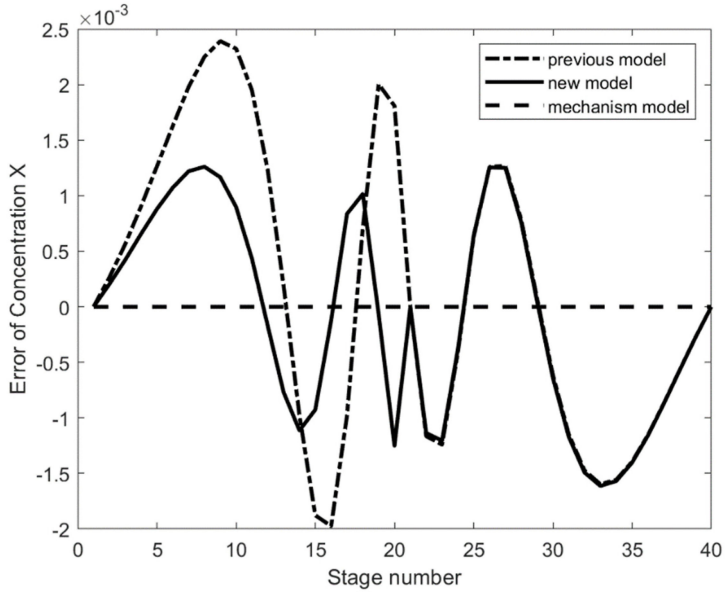

Figure 3. The concentration observation errors of the two models relative to the mechanistic model.

Overall, both models are significantly simplified compared to the mechanistic model. The nonlinear model based on mass transfer mechanisms has smaller concentration prediction errors than the wave model, indicating higher accuracy and competitive advantages.

3. Global Online Observer Design Based on Limited Measurements

The parameters in the description function of the concentration distribution curve are not constant during dynamic processes in the HIDiC, such as the variables mentioned earlier, including X_{r_max}, X_{r_min}, k, X_{s_max}, X_{s_min}, k_s, a_r, a_s, and more. Therefore, the required variables need to be estimated online. If conventional system identification methods are used, the temperature of each tray must still be measured, and the above parameters must be identified. Therefore, temperature sensors must be installed on each tray to obtain temperature information and subsequently derive concentration information for each tray, in practice. The new modeling method has not addressed the practical issue of requiring a large number of sensors. Therefore, an online observation method based on the new model was investigated. Without sacrificing accuracy excessively, model parameters can be identified through limited temperature information from trays to obtain all the necessary model information.

First, the number and locations that need to be observed are determined offline. Then, through real-time estimation of the relevant parameters and state variables using the

temperature information from the observation positions, we can estimate the real-time concentrations of each tray and predict the concentration changes of each tray.

3.1. Estimating Concentrations Based on Tray Temperatures

The concentrations inside the column are usually difficult to measure directly, while the temperatures can be easily obtained through corresponding sensors. Under certain conditions, the tray concentrations can be estimated from the respective tray temperatures. Therefore, different tray temperatures are investigated as the candidate measured variables.

In the benzene–toluene system, the tray concentration at each stage can be derived using the following formula.

According to the Antoine equation, the Raoult's law, and the Dalton's law, the heat-coupling relationship between trays is as follows:

$$T_j = b/(a - Lnp_{vp,j}) - c \tag{35}$$

$$p_{vp,j} = p/[X_j + (1 - X_j)/\alpha] \tag{36}$$

where a, b, c are the coefficients of the Antoine equation, $P_{vp,j}$ is the saturation vapor pressure of the j-th tray, and P represents the pressure of the column.

Through the above formulas, the corresponding functional relationship between the concentration and the temperature can be derived as follows:

$$X_j = (\alpha pe^{b/(T_j+c)-\alpha} - 1)/(\alpha - 1) \tag{37}$$

3.2. Selection of the First q Measuring Positions Based on PCA (Principal Component Analysis)

3.2.1. The Method for Selecting the Initial Observation Position

First, select the candidate tray positions that need to be observed based on the sensitivity matrix between the variables to be estimated and the temperatures of each tray. The elements of the sensitivity matrix are calculated as follows:

$$K_{ij} = \frac{\partial t_i/\bar{t}_i}{\partial p_i/\overline{p}_i} \tag{38}$$

where p represents the variable to be estimated, t represents the temperatures of each tray, and $\overline{p}$ and $\bar{t}$ represent the initial values of the corresponding variables, as shown in Table 1. A larger value of K_{ij} indicates that the temperature of the tray at that position has a greater impact on the variable to be estimated.

We use the covariance matrix calculation method from PCA (principal component analysis), and here we can define the covariance matrix corresponding to the sensitivity matrix as follows:

$$X = K^T K \tag{39}$$

Let λ_j represent the j-th eigenvalue of X, and P_{ij} denote the i-th element of the unit eigenvector corresponding to λ_j. By calculating the weighted sum of P_{ij} and λ_j, we obtain:

$$C_i = \frac{\sum_{j=1}^{q} |\lambda_j P_{ij}|}{\sum_{j=1}^{q} |\lambda_j|} \tag{40}$$

where $C_i \in [0\,1]$, and it represents the overall impact of the temperature of the i-th tray on the variable to be estimated. Therefore, the tray with the largest C_i can be selected as the first observation position.

3.2.2. Selection Method of the 2nd to the q-th Measurement Positions

Taking the rectifying section as an example, the variables to be measured are the parameters X_{r_max}, X_{r_min}, k_r, and a_r in the curve description function of the rectifying

section. With the number of variables to be measured, $q = 4$, the selection of the 2nd to q-th measurement positions can be determined using the following method:

Assume that m measurement positions have been selected and $1 \leq m < q$. The sensitivity vector $s_{k_l} = \left[K_{k_l 1}\ K_{k_l 2}\ \ldots\ K_{k_l q}\right], l \in [1\,m], k_l \in \left[1\ \frac{n}{2}\right]$. The sensitivity vectors $s_{k1}, s_{k_2}, \ldots, s_{k_\mathrm{m}}$ should be linearly independent; otherwise, terminate the algorithm. Then, in the m-dimensional vector space formed by the sensitivity vectors of $s_{k1}, s_{k_2}, \ldots, s_{k_\mathrm{m}}$, any vector $\hat{s}$ can be represented as:

$$\hat{s} = \sum_{l=1}^{m} \alpha_l s_{k_l} \tag{41}$$

where α_l is a constant. For any sensitivity vector s_i corresponding to an unselected tray, the vector $\hat{s}$ that is closest to s_i in the above m-dimensional vector space must satisfy:

$$\min_{a_l} \frac{1}{2}(s_i - \hat{s})^T (s_i - \hat{s}) \tag{42}$$

The sine of the angle between s_i and $\hat{s}$ can be represented as:

$$d_i = \sin\left[\cos^{-1}\left(\frac{s_i^T \hat{s}}{\|s_i\|\,\|\hat{s}\|}\right)\right] \tag{43}$$

The larger d_i is, the more independent information the corresponding measurement position can provide.

Therefore, we can define a sorting index $I_i = C_i d_i$, and the tray corresponding to the maximum I_i is chosen as the next measurement position. Since the dimension of vector s_{k_l} is q, this method can select q linearly independent sensitivity vectors, i.e., at most q measurement positions can be selected.

3.2.3. Selection for More Measurement Positions

If more measurement positions are needed, the goal is to select the next tray from those not yet chosen as measurement points. This tray should provide the maximum independent information. There may need to be more than the PCA method to select more than $q + 1$ linearly independent sensitivity vectors. Therefore, additional methods need to be employed on top of PCA.

The selection of the remaining measurement positions should consider two main aspects. First, trays with significant concentration changes should have an advantage in being selected, as larger concentration changes are more easily and accurately measured during dynamic processes. Second, trays close to each other are more likely to provide redundant information.

Therefore, it is not advisable to choose too many trays near the top and bottom of the column, where concentrations change relatively slowly. However, trays near the inflection points exhibit larger concentration differences, providing more independent information, and more measurement positions should be designed in those areas.

We take the rectifying section as an example and assume that a total of m measurement positions is needed. To complete the selection of the $q + 1$ to m measurement positions, a relative distribution index (RDI) is defined to meet the above two requirements:

$$D_i = \frac{\min\limits_{k_v}(|i - k_v|^\alpha)}{|i - S_1|^\beta} \tag{44}$$

where k_v represents the tray number, and $k_v \in \left[1\ \frac{n}{2}\right]$. v represents the existing number of measurements, and $v \in \left[q\ \frac{n}{2}\right]$. i represents the tray number not yet selected. S_1 represents the inflection point of the rectifying section, and α and β are weighting coefficients.

The numerator in the formula $\min\limits_{k_v}(|i - k_v|^\alpha)$ represents the dispersion of the evaluated tray. A larger value indicates that the evaluated tray is farther from other existing

measurement locations, providing more independent information and making it a priority for selection. The denominator $|i - S_1|^{\beta}$ represents the distance between this position and the inflection point. A larger value indicates that this position is far from the inflection point, closer to the top or bottom of the column, and less likely to be selected.

Therefore, the tray corresponding to the maximum D_i can be chosen as the following measurement location. This method can be iteratively used until all m measurement locations are determined.

3.2.4. Online Observation Design

As the products are produced at the top of the rectifying column and the bottom of the stripping column, respectively, the 1st and 40th trays are designated as product output locations, making them essential measurement locations. The measurement locations for other trays can be determined using the scheme described above.

The above measurement location scheme provides the required information for subsequent estimation of the model parameters. Since the situations in the rectifying section and the stripping section are similar, we will take the rectifying section as an example to derive relevant parameters based on solving the following optimization problem:

$$\begin{aligned} &\min_{X_{r\_\max}, X_{r\_\min}, k_r, a_r, S_1} \sum_{i=1}^{v} (\hat{X}_{k_v} - X_{k_v})^2 \\ &\text{Subject to :} \\ &k_v + \tfrac{1}{k_r}[(a_r + X_{r\_\max}) \ln(X_{r\_\max} - \hat{X}_{k_v}) - (a_r + X_{r\_\min}) \ln(\hat{X}_{k_v} - X_{r\_\min})] - S_1 = 0 \\ &X_{r\_\min} - X_{r\_\max} < 0 \\ &0 < X_{r\_\min} < 1 \\ &0 < X_{r\_\max} < 1 \end{aligned} \tag{45}$$

where k_v refers to the trays with measurements, X_{k_v} denotes the concentration values derived from the temperature measurements, and $\hat{X}_{k_v}$ represents the predicted concentration values. Subsequently, the tray concentrations without measurements can be estimated based on Equations (29) and (30).

It is necessary to evaluate the number of measurement positions to ensure the accuracy of predictions and the efficiency of measurements without redundancy. Using the operating conditions listed in Table 1 as simulation data, gradually increasing the number of measurement points in the rectifying and stripping sections; the root mean square error (RMSE) is used for error comparison:

$$RMSE = \sqrt{\frac{\sum_{j=1}^{n/2} (\hat{X}_j - X_j)}{n/2}} \tag{46}$$

We evaluate the errors of the two models (the wave model and the proposed model) separately and obtain the error metrics for different numbers of measurement points, as shown in Tables 2 and 3.

Table 2. RMSEs for the rectifying and stripping columns under different numbers of selected measurement trays by the wave model.

Section \ Measurement Number	3	4	5	6	7	20
Rectifying column	5.3×10^{-2}	1.5×10^{-2}	6.7×10^{-3}	3.9×10^{-3}	3.8×10^{-3}	3.5×10^{-3}
Stripping column	6.9×10^{-2}	2.2×10^{-2}	8.4×10^{-3}	3.3×10^{-3}	3.3×10^{-3}	3.2×10^{-3}

Table 3. RMSEs for the rectifying and stripping columns under different numbers of selected measurement trays by the proposed model.

Section \ Measurement Number	3	4	5	6	7	20
Rectifying column	4.3×10^{-2}	1.1×10^{-2}	5.6×10^{-3}	2.7×10^{-3}	2.7×10^{-3}	2.6×10^{-3}
Stripping column	4.9×10^{-2}	1.6×10^{-2}	7.4×10^{-3}	2.5×10^{-3}	2.5×10^{-3}	2.5×10^{-3}

From the error metrics, it is evident that, understandably, the concentration estimation error becomes smaller as the number of measurement points increases. After exceeding 6 measurement points, whether continuing to increase to 7 or when measuring all 20 trays, the reduction in errors becomes less significant. In both the rectifying and stripping sections, choosing 6 measurement points is a cost-effective option, considering the diminishing returns in error reduction. If other practical considerations, such as the possibility of inaccuracies in certain measurements or potential malfunctions, need to be taken into account, a slight increase in the number of measurement points could be considered. However, for the current analysis, considering 6 measurement points appears suitable. Finally, the measurement positions obtained according to the proposed selection method are shown in Table 4.

Table 4. Measurement ranking results for the rectifying and stripping columns.

Column \ Ranking	1st	2nd	3rd	4th	5th	6th
Rectifying column	1	20	19	16	8	13
Stripping column	40	31	26	29	23	37

4. Global Model and Dynamic Simulation Based on Limited Measurements

4.1. Global Model Based on Limited Measurements

Based on limited measurement points, the observer can derive the concentration information of all trays at the current moment with limited tray information, facilitating online monitoring of the overall situation of the HIDiC. By combining the established nonlinear model based on mass transfer mechanisms with the observer based on the limited measurement points, the current global information can be obtained, and future changes in concentrations can be predicted through the nonlinear model. The combination creates a global model that only requires limited measurement information, greatly enhancing the usability of the model. Taking the rectifying section as an example, the specific online model iteration strategy is as follows:

(1) Assuming the current moment is k, based on the tray information provided by the measurement points, the parameters ($X^k_{r\_\max}$, $X^k_{r\_\min}$, k^k_r, a^k_r, S^k_1) in the concentration curve distribution function can be solved using Equation (45), denoted as $p(k|k)$, where $p = [X_{r\_\max}, X_{r\_\min}, k_r, a_r, S_1]^T$;

(2) Substituting the parameters obtained in (1) into Equations (29) and (30), and assigning values to tray number j, can yield the concentration information for the corresponding tray. Consequently, various tray information, such as temperature, vapor–liquid molar flow, and more, can be obtained using Equations (1)–(10);

(3) Based on the model variables obtained in (2) and the proposed nonlinear model, the parameters for the concentration distribution function at the next step, denoted as $\hat{p}(k+1|k)$, can be predicted. Calculate the estimation error from the previous time step can be calculated and error compensation can be performed:

$$e(k) = p(k|k) - \widetilde{p}(k|k-1) \tag{47}$$

$$\widetilde{p}(k+1|k) = \hat{p}(k+1|k) + e(k) \tag{48}$$

where $\widetilde{p}(k+1|k)$ represents the predicted values of the model parameters after error compensation. Combine $\widetilde{p}(k+1|k)$ with the nonlinear model, the concentration changes of each tray at future time steps can then be predicted.

Through the above iterative computation, model parameters can be determined online. Based on the estimated values of model parameters and the nonlinear model, it is possible to predict the concentration changes for each tray in the HIDiC at future time points. The proposed method is especially useful for monitoring the concentrations in the first and nth trays, aiding in product quality control. Additionally, it provides convenience for the design and online application of subsequent control strategies.

4.2. Dynamic Simulation Results

The mechanistic model of the HIDiC was established using the MESH equations, which provide high accuracy. Therefore, this study uses the simulation results of the mechanistic model as a reference standard. With the involvement of the observer with limited measurement points, dynamic simulation experiments are conducted for both the wave model and the mass-transfer-based model. The results are then compared with those of the mechanistic model to validate the effectiveness of the proposed model. Simultaneously, the comparison between the two models can verify whether the proposed model exhibits higher accuracy.

The concentration prediction errors on four trays are chosen as representatives; the first and 40th trays represent the concentrations of the products at both ends, while the 16th and 31st trays represent trays relatively close to the inflection points in the rectifying and stripping sections.

Figure 4 illustrates the prediction errors of the two models under a 10% increase in the feed flow rate. The figure shows that the concentration prediction errors for the representative trays in the rectifying and stripping sections remain relatively small throughout the process. Specifically, both models exhibit small errors on the 1st and 40th trays, with the maximum error far below 10^{-4}. However, there is a significant difference between the two models on the intermediate trays. Taking the 16th tray as an example, the previous model initially shows a large positive error deviation of approximately 5×10^{-3}, followed by an even larger negative error deviation close to 6×10^{-3}. In contrast, the positive error of the new model is significantly smaller than that of the previous model, approximately 3×10^{-3}, with a very small negative error, rapidly converging to the vicinity of the final steady-state value. Since a biased estimation method is utilized in parameter identification, constraints are applied to minimize the deviations of the first and 40th trays. Consequently, the concentration prediction deviations for the first and 40th trays are relatively small and converge quickly. In the middle trays, the difference between the two models is more pronounced, with the model based on mass transfer mechanisms exhibiting superior predictive performance, indicating that the new model can significantly improve accuracy compared to the wave model.

Figure 5 shows the prediction errors of the two models under a 10% increase in the feed composition. The impact of the feed composition on the system's dynamics is more pronounced than that of the feed flow rate. Hence, the prediction errors in Figure 5 are significantly higher than those in Figure 4. In particular, both models exhibit very small errors on the 1st tray, of approximately 10^{-5}. The errors on the 40th tray are also relatively small. However, compared to the errors on the 1st tray, although the absolute magnitude of the errors does not show a significant increase, the convergence speed of the errors is slower. The errors on the intermediate trays are larger. Taking the 16th tray as an example, the final error of the previous model approaches -0.06, while the final error of the new model is slightly greater than -0.01. Although the errors of both models ultimately do not converge, the error rate of the new model is significantly smaller than that of the previous model. Both models can ensure error convergence at the two ends of the trays, but in the

middle trays, steady-state errors appear. The new model has smaller steady-state errors and faster convergence than the wave model.

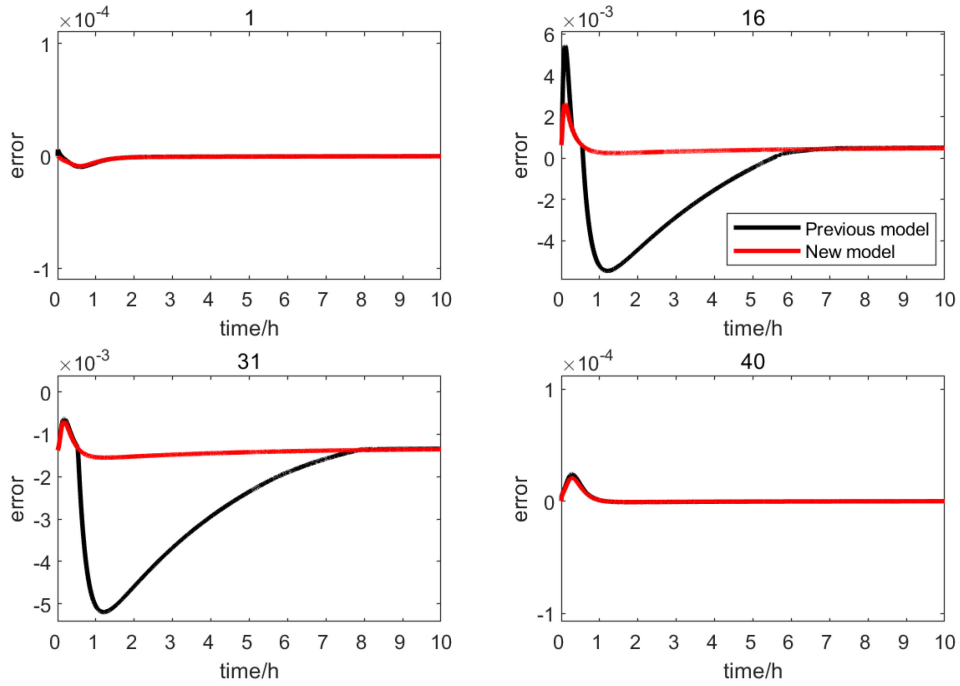

Figure 4. The dynamic prediction errors of tray concentrations under a 10% increase in the feed flow rate (F + 10%).

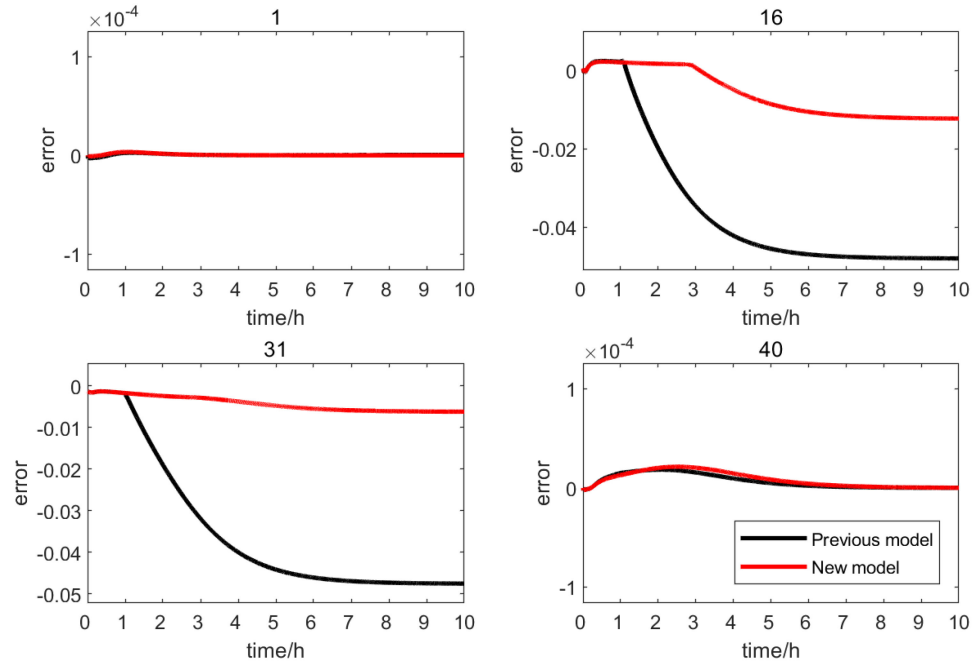

Figure 5. The dynamic prediction errors of tray concentrations under a 10% increase in the feed composition (Z_f + 10%).

Figure 6 presents the prediction errors of the two models under a 10% increase in the pressure of the stripping column. The impact of the pressure on the system's dynamics is similar to the feed flow rate changes. The overall magnitude of observation errors is generally within the range of 10^{-3} or smaller, and the final prediction results are essentially consistent with the concentrations from the mechanistic model. Moreover, the predictive

performance of the model, based on mass transfer mechanisms, is superior to that of the wave model, indicating the superiority of the new model's effectiveness.

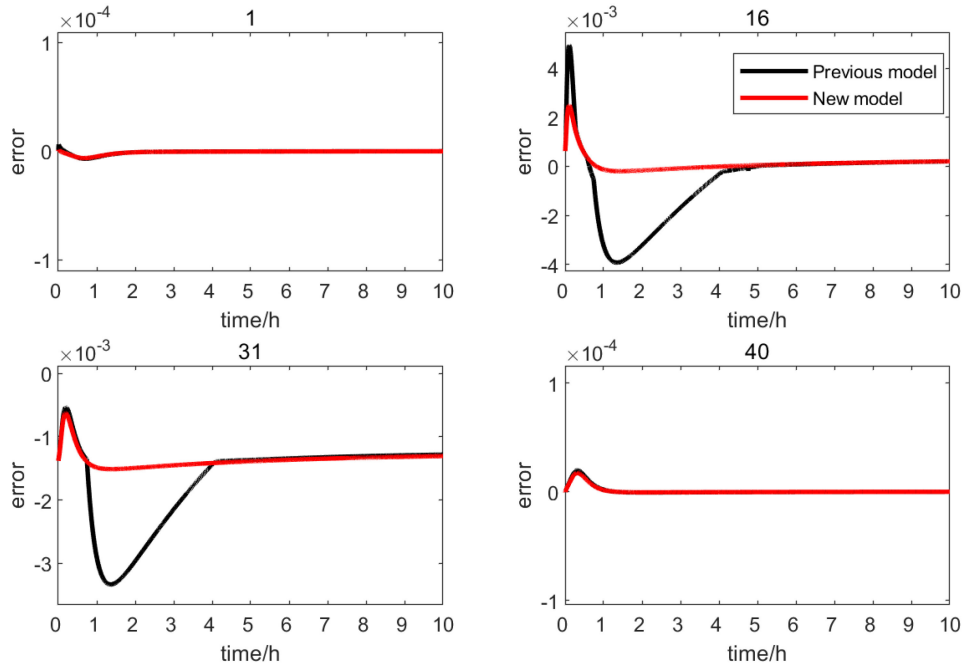

Figure 6. The dynamic prediction errors of tray concentrations under a 10% increase in the pressure of the stripping section (P_s + 10%).

5. Conclusions

The heat-integrated distillation column (HIDiC) is a novel energy-saving distillation technology. Due to its complex structure, strong coupling, and nonlinearity compared to traditional distillation column structures, there is a need for a high-precision and relatively simple model to assist in optimization design or online monitoring and control. Traditional mechanistic models are complex, and the previously proposed wave model requires improvement in accuracy. To address these issues, this paper introduces a high-precision nonlinear model based on mass transfer mechanisms. This model accurately characterizes the nonlinear characteristics of the distillation process and simplifies the model structure.

Furthermore, a method for designing a global observer based on limited local measurement points is proposed to overcome the drawback of requiring a large amount of state information for online applications of various HIDiC models. This observer constructs global tray information using only a limited number of tray temperature measurements. The observer first needs to determine, offline, the observation positions for the rectifying and stripping sections, ensuring that the observed variables of the selected trays sufficiently reflect the changes in various parameters in the model. It also ensures that the correlation between each observed variable is as tiny as possible and that each observation point contains as much independent information as possible. Then, the observer can estimate the model parameters online in the rectifying and stripping sections of the HIDiC and predict the concentration changes of each tray based on the limited measurements and the proposed model. The proposed method enables real-time monitoring of the HIDiC globally, and creates a novel global model based on limited measurement points.

Finally, simulation comparative experiments were conducted. The experimental results show that the proposed scheme can track the dynamic process changes of the HIDiC with high precision. Moreover, by comparing the results between the proposed model and the previous wave model, it is evident that the new model exhibits higher accuracy than the previous one. Therefore, the proposed approach can be well applied to online monitoring and control scheme design for distillation columns, providing a choice for subsequent model-based online research. Note that for other distillation processes, such as non-ideal

mixtures or different distillation columns, there may be a need to adjust the approximate form of the gas–liquid equilibrium relationship locally. Theoretically, the model accuracy may be slightly lower than that for ideal mixtures, but it should have significant advantages over other simplified modeling methods. Investigating modeling approaches for various distillation processes is our main focus for future work.

Author Contributions: Conceptualization, L.C.; methodology, L.C. and D.L.; software, D.L. and H.L.; validation, L.C. and D.L.; formal analysis, D.L.; investigation, L.C. and D.L.; writing—original draft preparation, D.L.; writing—review and editing, L.C. and H.L.; visualization, L.C.; supervision, L.C. All authors have read and agreed to the published version of the manuscript.

Funding: This work was supported by the Natural Science Foundation of Shandong Province, China (Grant ZR2022MB004) and the National Natural Science Foundation of China (Grant 21606255).

Data Availability Statement: The data presented in this study are available in the manuscript.

Conflicts of Interest: The authors declare no conflicts of interest.

References

1. Jana, A.K. Heat integrated distillation operation. *Appl. Energ.* **2010**, *87*, 1477–1494. [CrossRef]
2. Kiss, A.A. Distillation technology-still young and full of breakthrough opportunities. *J. Chem. Technol. Biot.* **2014**, *89*, 479–498. [CrossRef]
3. Tan, H.Y.; Cong, L. Modeling and Control Design for Distillation Columns Based on the Equilibrium Theory. *Processes* **2023**, *11*, 607. [CrossRef]
4. Zhao, Y.; Ma, K.; Bai, W.; Du, D.; Zhu, Z.; Wang, Y.; Gao, J. Energy-saving thermally coupled ternary extractive distillation process by combining with mixed entrainer for separating ternary mixture containing bioethanol. *Energy* **2018**, *148*, 296–308. [CrossRef]
5. Carrasco, B.; Avila, E.; Viloria, A.; Ricaurte, M. Shrinking-Core Model Integrating to the Fluid-Dynamic Analysis of Fixed-Bed Adsorption Towers for H2S Removal from Natural Gas. *Energies* **2021**, *14*, 5576. [CrossRef]
6. Liu, X.G.; Qian, J.X. Modeling, control, and optimization of ideal internal thermally coupled distillation columns. *Chem. Eng. Technol.* **2000**, *23*, 235–241. [CrossRef]
7. Zhu, Y.; Liu, X.G. Dynamics and control of high purity heat integrated distillation columns. *Ind. Eng. Chem. Res.* **2005**, *44*, 8806–8814. [CrossRef]
8. Chen, H.S.; Huang, K.J.; Wang, S.F. A novel simplified configuration for an ideal heat-integrated distillation column (ideal HIDiC). *Sep. Purif. Technol.* **2010**, *73*, 230–242. [CrossRef]
9. Jana, A.K. Performance analysis of a heat integrated column with heat pumping. *Sep. Purif. Technol.* **2019**, *209*, 18–25. [CrossRef]
10. Gu, J.; Lu, S.; Shi, F.; Wang, X.; You, X. Economic and Environmental Evaluation of Heat-Integrated Pressure-Swing Distillation by Multiobjective Optimization. *Ind. Eng. Chem. Res.* **2022**, *61*, 9004–9014. [CrossRef]
11. Zhu, Z.; Li, S.; Dai, Y.; Yang, X.; Wang, Y.; Gao, J. Control of a pressure-swing distillation process for benzene/isopropanol/water separation with and without heat integration. *Sep. Purif. Technol.* **2020**, *236*, 116311. [CrossRef]
12. Wang, N.; Ye, Q.; Ren, X.; Chen, L.; Zhang, H.; Fan, Y.; Cen, H.; Zhong, J. Performance Enhancement of Heat Pump with Preheater-Assisted Pressure-Swing Distillation Process. *Ind. Eng. Chem. Res.* **2020**, *59*, 4742–4755. [CrossRef]
13. Zhu, S.; Yang, A.; Kong, Z.Y.; Sun, S.; Bai, M.; Sunarso, J. Control of heat-integrated indirect triple-column extractive distillation for separating ternary azeotropic mixture tetrahydrofuran-ethyl acetate-water. *Sep. Purif. Technol.* **2023**, *308*, 122951. [CrossRef]
14. Ye, Q.; Wang, Y.; Pan, H.; Zhou, W.; Yuan, P. Design and Control of Extractive Dividing Wall Column for Separating Dipropyl Ether/1-Propyl Alcohol Mixture. *Processes* **2022**, *10*, 665. [CrossRef]
15. Cantero, C.A.T.; Perez Zuniga, R.; Martinez Garcia, M.; Ramos Cabral, S.; Calixto-Rodriguez, M.; Valdez Martinez, J.S.; Mena Enriquez, M.G.; Perez Estrada, A.J.; Ortiz Torres, G.; Sorcia Vazquez, F.d.J.; et al. Design and Control Applied to an Extractive Distillation Column with Salt for the Production of Bioethanol. *Processes* **2022**, *10*, 1792. [CrossRef]
16. Shi, T.; Chun, W.; Yang, A.; Su, Y.; Jin, S.; Ren, J.; Shen, W. Optimization and control of energy saving side-stream extractive distillation with heat integration for separating ethyl acetate-ethanol azeotrope. *Chem. Eng. Sci.* **2019**, *215*, 115373. [CrossRef]
17. Zhang, P.K.; Liang, J.Y.; Yang, Y.H.; Wang, L. A new heating system for the air pre-purification of air separation units. *Appl. Therm. Eng.* **2023**, *226*, 120194. [CrossRef]
18. Cong, L.; Chang, L.; Liu, X.; Deng, X.; Chen, H. Analysis of CO_2 Emission and Economic Feasibility for a Heat-Integrated Air Separation System. *Chem. Eng. Technol.* **2018**, *41*, 1639–1648. [CrossRef]
19. Chang, L.; Liu, X. Non-equilibrium stage based modeling of heat integrated air separation columns. *Sep. Purif. Technol.* **2014**, *134*, 73–81. [CrossRef]
20. Cong, L.; Li, X. Reduced-Order Modeling and Control of Heat-Integrated Air Separation Column Based on Nonlinear Wave Theory. *Processes* **2023**, *11*, 2918. [CrossRef]
21. Hsiao, T.-L.; Weng, K.-C.; Lee, H.-Y. Design and control of hybrid heat-integrated configuration for an ideal indirect reactive distillation process. *J. Taiwan. Inst. Chem. E.* **2017**, *73*, 37–49. [CrossRef]

22. Jana, A.K.; Maiti, D. An ideal internally heat integrated batch distillation with a jacketed still with application to a reactive system. *Energy* **2013**, *57*, 527–534. [CrossRef]
23. Gao, X.; Yang, Y.; Chen, M.; Cheng, Q.; Lu, K. Study on a novel reactive internally heat integrated distillation process for the synthesis of ethyl acetate and its column configuration. *Sep. Purif. Technol.* **2022**, *300*, 121755. [CrossRef]
24. Gao, X.; Weng, X.; Yang, Y.; Zhou, Z. Partial heat-integrated reactive distillation process for producing n-propyl acetate using a heat exchanger network. *Energy Sources Part A Recovery Util. Environ. Eff.* **2024**, *46*, 2284–2298. [CrossRef]
25. Kiss, A.A.; Olujic, Z. A review on process intensification in internally heat-integrated distillation columns. *Chem. Eng. Process.-Process Intensif.* **2014**, *86*, 125–144. [CrossRef]
26. Nakaiwa, M.; Huang, K.; Endo, A.; Ohmori, T.; Akiya, T.; Takamatsu, T. Internally heat-integrated distillation columns: A review. *Chem. Eng. Res. Des.* **2003**, *81*, 162–177. [CrossRef]
27. Cong, L.; Liu, X. Nonlinear-Model-Based Control of a Heat Integrated Distillation Column Using Model Updating Based on Distributed Wave Velocity. *Ind. Eng. Chem. Res.* **2019**, *58*, 20758–20768. [CrossRef]
28. Luyben, W.L. Control of heat-integrated extractive distillation processes. *Comput. Chem. Eng.* **2018**, *111*, 267–277. [CrossRef]
29. Huang, K.; Nakaiwa, M.; Akiya, T.; Aso, K.; Takamatsu, T. A numerical consideration on dynamic modeling and control of ideal heat integrated distillation columns. *J. Chem. Eng. Jpn.* **1996**, *29*, 344–351. [CrossRef]
30. Eyvazi-Abhari, N.; Khalili-Garakani, A.; Kasiri, N. Reaction/distillation matrix algorithm development to cover sequences containing reactive HIDiC: Validation in optimized process of dimethyl carbonate production. *Energy* **2023**, *276*, 127493. [CrossRef]
31. Gao, X.; Wang, F.; Li, H.; Li, X. Heat-integrated reactive distillation process for TAME synthesis. *Sep. Purif. Technol.* **2014**, *132*, 468–478. [CrossRef]
32. Wang, Y.; Qi, P.; Yang, X.; Zhu, Z.; Gao, J.; Zhang, F. Exploration of a heat-integrated pressure-swing distillation process with a varied-diameter column for binary azeotrope separation. *Chem. Eng. Commun.* **2019**, *206*, 1689–1705. [CrossRef]
33. Li, X.; Geng, X.; Cui, P.; Yang, J.; Zhu, Z.; Wang, Y.; Xu, D. Thermodynamic efficiency enhancement of pressure-swing distillation process via heat integration and heat pump technology. *Appl. Therm. Eng.* **2019**, *154*, 519–529. [CrossRef]
34. Wang, X.; Xie, L.; Tian, P.; Tian, G. Design and control of extractive dividing wall column and pressure-swing distillation for separating azeotropic mixture of acetonitrile/N-propanol. *Chem. Eng. Process.-Process Intensif.* **2016**, *110*, 172–187. [CrossRef]
35. Quarshie, A.W.K.; Swartz, C.L.E.; Madabhushi, P.B.; Cao, Y.N.; Wang, Y.J.; Flores-Cerrillo, J. Modeling, simulation, and optimization of multiproduct cryogenic air separation unit startup. *AIChE J.* **2023**, *69*, e17953. [CrossRef]
36. Mora, C.A.; Orjuela, A. Modeling, validation and exergy evaluation of a thermally-integrated industrial cryogenic air separation plant in Colombia. *Chem. Eng. Res. Des.* **2022**, *185*, 73–86. [CrossRef]
37. Yan, Z.B.; Liu, X.G. Modeling and Behavior Analyses of Internal Thermally Coupled Air Separation Columns. *Chem. Eng. Technol.* **2011**, *34*, 201–207. [CrossRef]
38. Cong, L.; Liu, X.; Deng, X.; Chen, H. Development of a partially accurate model and application to a reduced-order control scheme for heat integrated distillation column. *Sep. Purif. Technol.* **2019**, *229*, 115809. [CrossRef]
39. Marquardt, W.; Amrhein, M. Development of a Linear Distillation Model from Design-Data for Process-Control. *Comput. Chem. Eng.* **1994**, *18*, S349–S353. [CrossRef]